Available online at www.sciencedirect.com

ScienceDirect

Procedia CIRP 112 (2022) 346–351

www.elsevier.com/locate/procedia

15th CIRP Conference on Intelligent Computation in Manufacturing Engineering, Gulf of Naples, Italy

Multi-material additive manufacturing of thermocouples by laser-based powder bed fusion

Christopher Singer[a,*], Matthias Schmitt[a], Georg Schlick[a], Johannes Schilp[a,b]

[a]*Fraunhofer IGCV (Research Institute for Casting, Composite and Processing Technology), Am Technologiezentrum 10, 86159 Augsburg*
[b]*University of Augsburg, Chair of Digital Manufacturing, Department of Applied Computer Science, Universitätsstraße 2, 86159 Augsburg, Germany*

* Corresponding author. Tel.: +49-821-90678-330; fax: +49-821-90678-0. *E-mail address:* christopher.singer@igcv.fraunhofer.de

Abstract

Multi-material additive manufacturing by laser-based powder bed fusion (PBF-LB) enables arbitrary material composition in components and thus enables the manufacturing of so-called smart parts. By combining different materials sensoric structures can be implemented into components. This paper investigates the possibilities to manufacture thermocouples (TC) consisting of two nickel-based alloys by the means of PBF-LB. These alloys are qualified to achieve sufficient relative densities for the thermocouples. Furthermore, the electrical conductivity of the parts is measured and compared to literature values. Finally, additively manufactured thermocouples are tested in comparison to conventional thermocouples in the temperature range from 50 to 350 °C.

Keywords: metal additive manufacturing; sensor printing; thermocouples; smart parts; laser-based powder bed fusion; laser beam melting; multi-material

1. Introduction

Recent megatrends as digital monitoring and predictive maintenance increase the demand for components with integrated sensors. Multi-material additive manufacturing provides new opportunities for functional integration beyond the state of the art [1-2]. One promising possibility is the manufacturing of sensors and mechanical parts in one process. This paper describes the process to manufacture thermocouples by the means of powder bed fusion (PBF) of metallic multi-material (/MM) using a laser beam (-LB) (PBF-LB/MM).

As PBF-LB is a powder bed-based process, the standard process has to be adapted to manufacture 3-D-multi-material parts. The approaches for PBF-LB/MM are differentiated into selective and full-surface applications. In research, PBF-LB/MM has been shown to work with powder application using nozzles, modified recoaters with suction modules or drums with pressurized air [3-6].

The manufacturing of sensors has already been demonstrated for other metal additive manufacturing processes where multi-material manufacturing can be realised with less effort. For laser cladding, Zhang et al. demonstrated the successful fabrication of type K thermocouples [7]. Other additive manufacturing processes where thermocouples have been successfully manufactured include screen printing and laser-induced forward printing [8-9].

For PBF-LB, the integration of sensors into additively manufactured parts has been demonstrated. Different sensors like strain gauges, fibre bragg and PT-100 sensors could be successfully integrated into parts [10-12]. The direct manufacturing of sensors using PBF-LB/MM has yet to be shown. Compared to the integration, the additive manufacturing of sensors allows for a free orientation in the part as well as a better bonding in terms of thermal conductivity.

Thermocouples are temperatures sensors consisting of a joint of two dissimilar metals. Due to the thermoelectric effect, a temperature-dependent voltage between the two legs of the thermocouple can be measured. The simple working principle and structure of thermocouples make them an obvious choice

2212-8271
10.1016/j.procir.2022.09.007

for additively manufactured sensors. Different types of thermocouples are standardized in the DIN EN 60584 [13]. In this paper, a multi-material process to manufacture type K Thermocouples consisting of Ni90Cr10 (known as chromel) and Ni95AlMnSi (known as alumel) is described.

Nomenclature

E_v	volumetric energy density (J/mm³)
E_L	linear energy density (J/mm)
P	laser power (W)
v_s	scan velocity (mm/s)
d	melt pool depth (µm)
h	hatch distance (µm)
t	layer thickness (µm)
σ	electrical conductivity (S/m)
ρ	relative density (%)
T	temperature (°C)

2. Experimental equipment and material

The specimens including the single tracks as well as cubes were manufactured on a 50 x 50 mm² substrate platform in an MTT SLM 250^{HL}, which has a modified recoater with a suction module for PBF-LB/MM. The pictures of the single tracks were taken with a laser microscope of the type Keyence VX-9700. The microscope images of the specimens were taken with an Olympus BX53M. For the measurement of the melt pool dimensions of the single tracks, the specimens were etched for 20 seconds with 5% nitric acid (5% HNO_3). The measurement of the electrical conductivity was performed using a RESISTIVITY METER LORESTA GX from Mitsubishi Chemical Analytech. The two nickel-based alloys were purchased from Sandvik Osprey Ltd. (chemical composition is given in Table 1).

Table 1. Chemical composition of the powder materials according to the supplier certificate.

Alloy	Ni (wt.-%)	Cr (wt.-%)	Mn (wt.-%)	Al (wt.-%)	Si (wt.-%)
Ni90Cr10	Balance	9.8	-	-	-
Ni95AlMnSi	Balance	-	2.0	1.7	0.94

3. Results and Discussion

3.1 Preliminary Parameter study

Since Ni90Cr10 and Ni95AlMnSi had not been processed by PBF-LB before, suitable parameters had to be qualified. There are different approaches to investigate the processability of alloys for PBF-LB. One of them is to analyse the geometry and dimensions of single tracks exposed to substrate plates of the respective materials with different laser powers and scan velocities. Since there are no substrate plates commercially available for chromel and alumel, the first step was to identify suitable parameters to produce specimens with a sufficient relative density for further investigations.
With Inconel 718 (IN718) being a nickel-based alloy with a content of 50 – 55 wt.-% nickel, the parameters for this alloy on the same PBF-LB machine were used as a starting point. The seven resulting parameter sets yielding to volumetric energy densities (for definition of volumetric and linear energy density see [14]) lower and higher than for IN718 are listed in Table 2 (parameters for IN718 are 220 W laser power, 800 mm/s scan velocity, and 125 µm hatch distance). The hatch distance and layer height are 125 µm and 30 µm for all cubes.

Table 2.Parameter sets for the first set of cubes.

P (W)	v_s (mm/s)	E_v (J/mm³)
100	650	41.03
150	650	61.54
150	750	53.33
150	850	47.05
150	950	42.11
200	750	71.11
200	850	62.75

The manufactured cubes had dimensions of 10 x 10 x 10 mm³. The relative density of the cubes was determined using Archimedes' principle. In Fig. 1, the relative density over the volumetric energy density is shown. For both alloys, the relative density follows the same trend. For energy densities between 40 to 55 J/mm³ the relative density of both alloys increases strongly with increasing energy density. For high energy densities between 55 to 70 J/mm³ the gradient of the curve decreases. The highest relative density is achieved with a laser power of 200 W and a scan velocity of 750 mm/s. With the respective parameters, alumel reaches a relative density of 97% and chromel of 98%. These relative densities were sufficient to built basic cubes for subsequent single tracks on top.

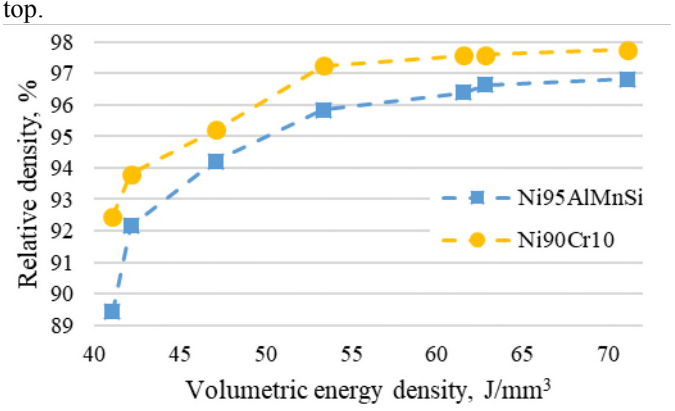

Fig. 1: Relative density of alumel and chromel cubes manufactured with varied volumetric energy density

3.2 Single Tracks

With these parameters, 30 cubes with the dimension of 5 x 5 x 5 mm were manufactured. On top of each cube, three single tracks were built in a distance of 1 mm using fixed laser power and scan velocity. The laser power was varied between 150 and 400 W in 50 W steps and the scan velocity between 300 and 1100 mm/s in 200 mm/s steps. This yields to 90 single tracks with 30 different parameter sets. To investigate the geometry of the single tracks images were taken from the top of the cubes using laser microscopy. In Fig. 2 an overview of the single track images is shown (the single tracks for 1100 mm/s are omitted for better visibility).

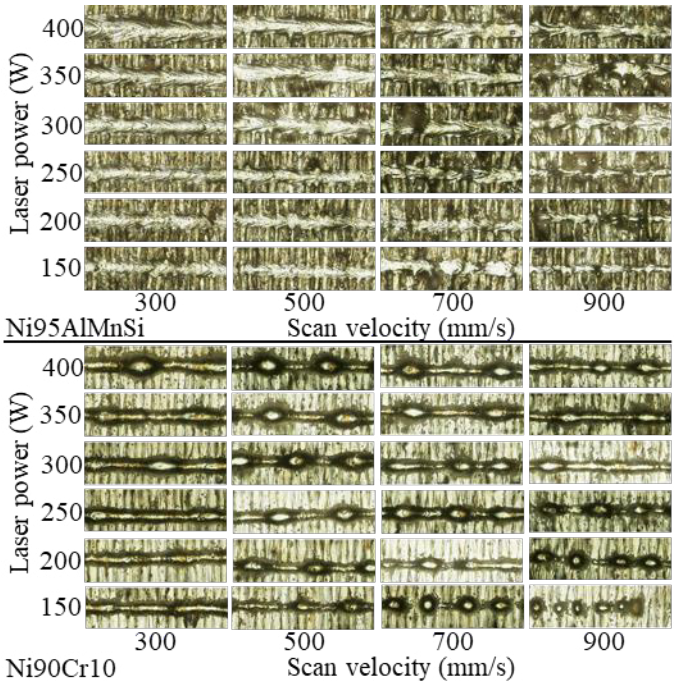

Fig. 2: Laser microscope images of alumel and chromel single tracks between 150 and 400 W as well as 300 and 900 mm/s with a length of approx. 2mm

For chromel, we observe pronounced balling effects for low linear energy densities. These balling effects lead to irregularly shaped tracks where parts of the track are wider and higher than the remaining track, For the manufacturing of 3-D parts this should be prevented since balling effects are an indicator for too low energy input and could lead to bonding defects [15]. In contrast, alumel does not show balling effects for the investigated parameters.

For a combination of high scan velocities and low laser powers interruptions in the single track can be observed, e. g. for the chromel track with 150 W and 900 mm/s. This indicates a collapsing melt pool during the process. Since this leads to incomplete melting of the powder and insufficient bonding between the layers these parameters are excluded for further investigations. This effect is more pronounced for chromel but is also observed for alumel. In general, the single tracks are wider for lower scan velocities and higher laser powers.

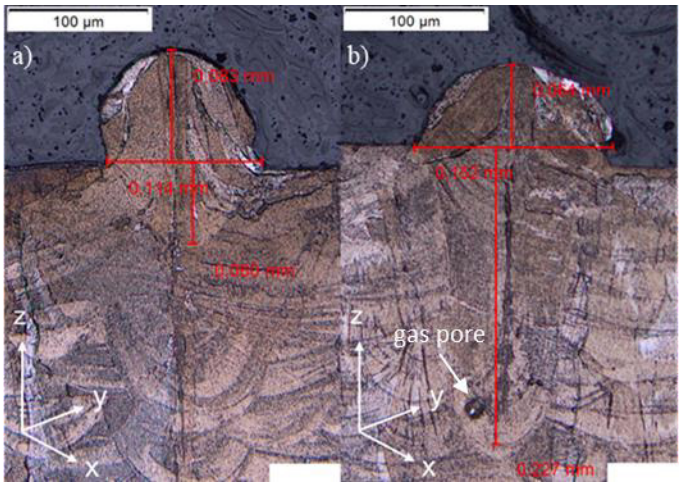

Fig. 3: Microscope images of chromel single track cross-sections with different parameter sets: a) 150 W, 700 mm/s, b) 200 W, 300mm/s

Metallographic crosssection of the cubes were prepared to measure the melt pool dimensions of the single tracks. In the images taken with a light microscope the melt pool depth, width and the track height on top of the cube were measured. In Fig. 3 two examples of single track cross-sections for chromel sections are given.

Furthermore, an evaluation whether the parameters lead to a conduction or keyhole mode welding was conducted. As a definition, a melt pool depth which is deeper than the according melt pool width is considered a keyhole type melt pool geometry [16]. In addition, the overall shape and the occurrence of gas pores at the lower end of the melt pool indicate the transition from conduction to keyhole mode welding. Fig. 3 a) shows an example for a typical conduction mode melt pool geometry while Fig. 3 b) inhibits keyhole mode characteristics like a gas pore and a relatively deep melt pool.

When plotting the melt pool depth over the linear energy density as depicted in Fig. 4 a) and b) the data points show a linear dependency for both alloys. With increasing linear energy densities, the melt pool depth increases as well. The linear fits for the data show an accurate R^2-Value of 0.97 for alumel and 0.94 for chromel. A clear cut-off between conduction and keyhole mode can be located between 0.44 J/mm and 0.5 J/mm.

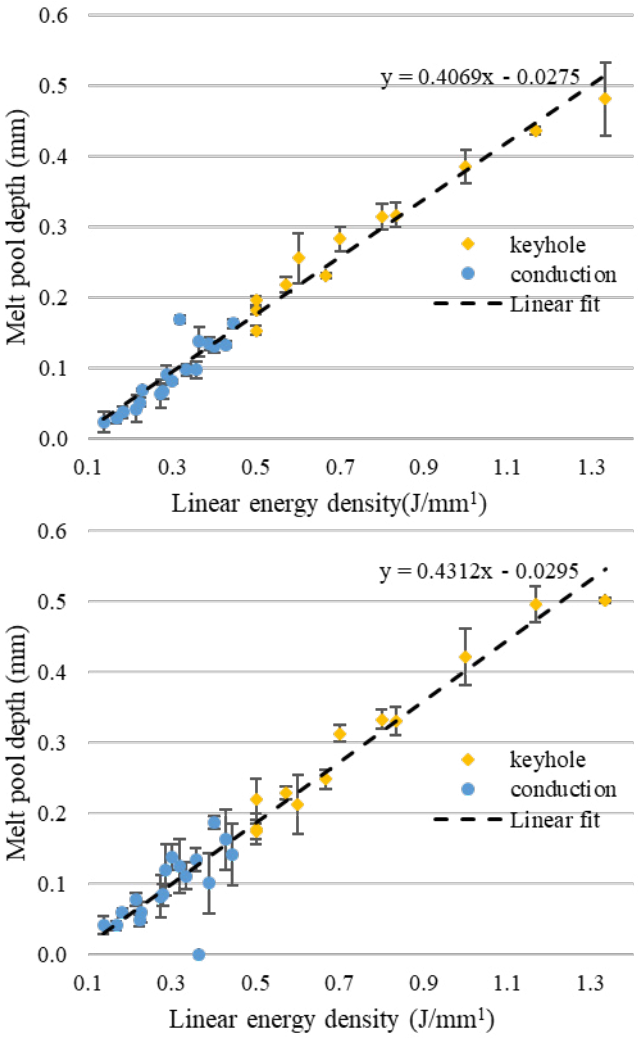

Fig.4: Melt pool depth over linear energy density for chromel (top) and alumel (bottom)

3.3. Final parameter study

Taking into consideration the melt pool depth, the cut-off between conduction and keyhole mode as well as the qualitative evaluation of the laser microscope images three different parameter combinations of laser power and scan velocity were chosen for the manufacturing of a second set of cubes. The parameter sets have linear energy densities below 0.5 J/mm. Thus, keyhole mode and consequently gas pores should not occur. Additonally, comparatively high scan velocities were chosen to minimize the built time. The resulting melt pool depth for the three chosen parameters are deep enough to re-melt underlying layers during the process, which should result in a sufficient bonding between the layers. As an additional parameter, the hatch distance was varied from 85 – 125 µm. The layer height was kept constant at 30 µm. For each alloy nine cubes were manufactured with the parameters listed in Table 3 and Table 4 together with the achieved relative density and electrical conductivity

Table 3. Parameter sets, relative density and electrical conductivity for the second set of chromel cubes

P (W)	v_s (mm/s)	h (µm)	ρ (%)	σ (S/µm)
200	700	85	99.378	1.51
200	700	105	99.753	1.49
200	700	125	99.390	1.50
350	900	85	99.571	1.52
350	900	105	99.716	1.51
350	900	125	99.302	1.50
400	900	85	99.591	1.51
400	900	105	99.487	1.54
400	900	125	99.978	1.48

Table 4.Parameter sets, relative density and electrical conductivity for the second set of alumel cubes.

P (W)	v_s (mm/s)	h (µm)	ρ (%)	σ (S/µm)
250	900	85	97.701	3.46
250	900	105	97.907	3.38
250	900	125	97.657	3.45
200	700	85	97.230	3.36
200	700	105	97.073	3.42
200	700	125	97.219	3.42
400	900	85	97.754	3.34
400	900	105	97.544	3.39
400	900	125	97.885	3.38

Again, the relative density of the cubes was measured using Archimedes' principle. For chromel the relative density exceeds 99% for all chosen parameter sets. The highest relative density with 99.978% was achieved with a laser power of 400 W, a scan velocity of 900 mm/s and a hatch distance of 125 µm. For alumel the relative density was below 98% for all cubes. The highest relative density of 97.885% was achieved with the same parameters as for chromel. Cross-sections of the specimens with the highest relative densities are depicted in Fig. 5. For chromel in Fig. 5 a) pores are mainly seen at the edges of the specimen. This is probably due to the missing exposure of a contour. The heat conductivity at the edges of the cubes are lower because of the surrounding powder possibly leading to gas pores. Alumel in Fig. b) shows additional pores evenly distributed over the whole cross-section of the specimen. The occurrence of gas pores leads to the assumption that the volume energy densities of the parameter combinations were to high.

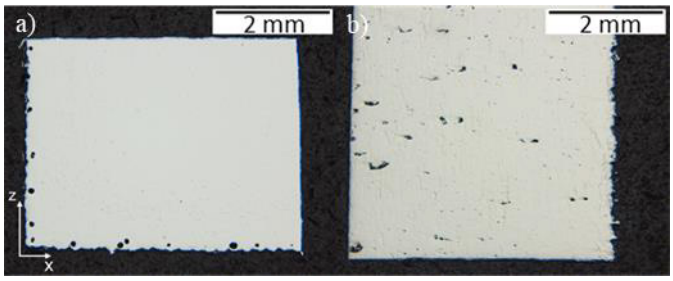

Fig. 5: cross-section images of chromel (a) and alumel (b) cubes (Parameters: 400 W, 900 mm/s, 125 µm)

Furthermore, the electrical conductivity of each specimen was measured using the 4-point method. The electrical conductivity can be used as a measure for the thermoelectric performance of the thermocouples, which depends on thermal and electrical conductivity. The literature values for the electrical conductivity are 1.42 S/µm for chromel and 3.4 S/µm for alumel. The measured electrical conductivity is slightly higher than the literature values. Reasons could be uncertainties in the measurement setup and the manual measurement of the dimensions of the cubes. Overall, the values seen in Tables 3 and 4 are in good accordance with these literature values. For alumel the rather low relative density does not affect the electrical conductivity.

3.4 Multi-material processing & thermoelectric performance

For the multi-material processing of the type K thermocouple the parameter set of 400 W, 900 mm/s and 125 µm was chosen for both alloys. To take into account possible anisotropic properties due to the layer-wise structure of additively manufactured parts two thermocouples were built with one lying on the substrate plate while the second was built in upright position. The two manufactured thermocouples are shown in Fig. 6.

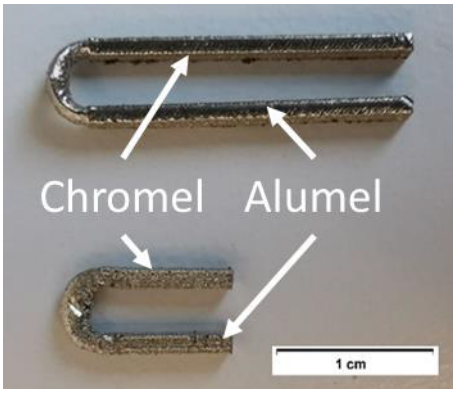

Fig. 6: Picture of the lying (top) and standing (bottom) additively manufactured thermocouples

For the testing of the thermoelectric performance of the thermocouples, an experiment with a conventional type K thermocouple in an oven was set up. The temperature for both thermocouples was tracked over a temperature range of 50 to 350 °C. The oven temperature was kept constant at 50 °C intervals (50, 100, 150 °C, …) to guarantee a homogeneous temperature distribution through the thermocouple.
The temperature of the two additively manufactured thermocouples (AM-TC) over the temperature of the conventional thermocouple is shown in Fig. 7. For comparison, the linear fits are added. A perfect agreement with the conventional thermocouple would lead to a linear function with a slope of 1 and an axis intercept of 0. Both AM-TCs exhibit very small deviation in the measured temperature compared to the conventional thermocouple. The average deviation over the complete temperature range amounts to 0.2 °C for the lying and 0.6 °C for the standing AM-TC respectively. Taking into account the measurement deviation from the conventional TC, which varies between 1 and 2 °C, the temperature measurement of the AM-TC is in good agreement with the conventional TC.

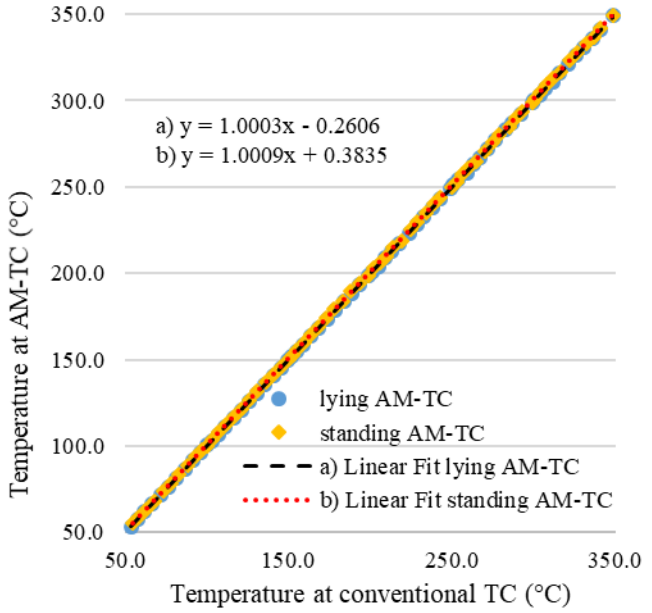

Fig. 7: Measured temperatures for lying and standing AM-TC over measured temperature of a conventional TC from 50 – 350 °C

4. Conclusion and Outlook

In this paper, the successful manufacturing of thermocouples using PBF-LB/MM is demonstrated. The following results can be summarized:

- The approach of using single tracks for processing new materials in L-PBF is appropriate to investigate the melt pool behaviour and resulting track geometries.
- A defined cut-off between conduction and keyhole mode in terms of linear energy density was found and was successfully used to determine promising parameters for three dimensional geometries.
- Parameters achieving a high relative densitiy of 99.978 % for chromel but comparatively low relative densitiy of 97.885 % for alumel could be identified. However, electrical conductivity was not affected by the low relative density.
- PBF-LB/MM is suitable for manufacturing thermocouples showing comparable results to conventional TCs. The type K AM-TCs show very good temperature correlation even if the relative densities for alumel only reach values between 97 and 98%

Looking at further research demands, the following topics need to be investigated in more detail:

- Type K thermocouples are principally suitable for temperatures up to 1,100 °C. The AM-TC should therefore be tested up to this temperature
- The implementation of AM-TCs into parts requires the use of three to four materials considering an insulating as well as a structural material. Therefore, the approaches for PBF-LB/MM have to be advanced to process more than two materials.
- The combination of the thermocouple materials with an insulating material needs to be studied. Processing insulating materials in L-PBF is challenging and the combination with metals produces even more challenges possibly leading to a decrease of the thermoelectric performance.
- Further investigations should consider geometric restraints and factors for manufacturing TCs using PBF-LB/MM.

Acknowledgements

The authors express their sincere thanks to the European Commision, EUREKA and the Federal Ministry of Education and Research in Germany (BMBF) for funding the project MMAM-Flow (Multi-material additive manufacturing for advanced flow probes). Furthermore, the authors thank Norbert Zimmer for the support in conducting the experiments as well as Andreas Machnik and Bram Neirinck for the advices and discussion regarding addtively manufactured thermocouples.

References

[1] Wohlers Associates, Wohlers Report 2020: 30 Printing and Additive Manufacturing Global State of the Industry, Colorado, (2020).
[2] M. Binder, L. Kirchbichler, C. Seidel, C. Anstaett, G. Schlick, G. Reinhart, Design Concepts for the Integration of Electronic Components into Metal Laser-based Powder Bed Fusion Parts, Procedia CIRP 81 (2019) 992–997.
[3] S. Girnth, J. Koopmann, G. Klawitter, N. Waldt, T. Niendorf, 3D hybrid-material processing in selective laser melting: implementation of a selective coating system, Progress in Additive Manufacturing (2019) 4:399 – 409.
[4] C. Anstätt, C.Seidel, G. Reinhart, Multi-material Processing in Laser Beam Melting, Fraunhofer Direct Digital Manufacturing Conference; Fraunhofer-Allianz Generative Fertigung; DDMC (2016): Fraunhofer Direct Digital Manufacturing Conference 2016 proceedings.
[5] C. Anstätt, C. Seidel, G. Reinhart, Fabrication of 3D Multi-material Parts Using Laser-based Powder Bed Fusion, Proceedings of the 28th Annual International Solid Freeform Fabrication Symposium (2017).
[6] M. Rafiee, R. D. Farahani, D. Therriault, Multi-Material 3D and 4D Printing: A Survey, In: Advanced Science 7 (12), (2020) S. 1902307
[7] Y. Zhang, D. Mack, G. Mauer, R. Vaßen, Laser Cladding of Embedded Sensors for Thermal Barrier Coating Applications, In: Coatings 8 (5), (2018) S. 176.
[8] J. Luo, R. Pohl, L. Qi, G.-W. Römer, C. Sun, D. Lohse, C. W. Visser, Printing Functional 3D Microdevices by Laser-Induced Forward Transfer, In: Small (Weinheim an der Bergstrasse, Germany) 13 (9), (2016).
[9] Y. Liu, W. Ren, P. Shi, D. Liu, Y. Zhang, M. Liu, Z. Ye, W. Jing, B. Tian Z. Jiang, A Highly Thermostable In2O3/ITO Thin Film Thermocouple Prepared via Screen Printing for High Temperature Measurements, Sensors, 18, 958 (2018).

[10] P. Stoll, J. Mathew, A. Spierings, Bauer Thomas, R. Maier, Embedding fibre optical sensors into SLM parts, Proceedings of the 27th Annual International Solid Freeform Fabrication Symposium (2016).
[11] M. Binder, M. Fischer, S. Dietrich, C. Seidel, G. Reinhart, Integration of Strain Gauges in Components Manufactured by Laser-Based Powder Bed Fusion, MIC Procedia (2020) 034–04.
[12] M. Binder, L. Kirchbichler, C. Seidel, C. Anstätt, G. Schlick, G. Reinart, Design Concepts for the Integration of Electronic Components into Metal Laser-based Powder Bed Fusion Parts. In: Procedia CIRP 81, S. 992–997.
[13] DIN EN 60584-1:2014-07, Thermoelemente – Teil 1: Thermospannungen und Grenzabweichungen (IEC 60584-1:2013); Deutsche Fassung EN 60584-1:2013.
[14]J. Zhu, E. Borisov, X. Liang, E. Farber, M. J. M Hermans, V. A. Popovich, V. A., Predictive analytical modelling and experimental validation of processing maps in additive manufacturing of nitinol alloys. In: Additive Manufacturing 38 (2021) 101802.
[15] N. W. Makoana, I. Yadroitsava, H. Möller, I. Yadroitsev, Characterization of 17-4PH Single Tracks Produced at Different Parametric Conditions towards Increased Productivity of LPBF Systems—The Effect of Laser Power and Spot Size Upscaling, In: Metals 8(7), (2018) 475
[16] U. Scipioni Bertoli, A. J. Wolfer, M. J. Matthews, Delplanque, R. Jean-Pierre, J. M. Schoenung, On the limitations of Volumetric Energy Density as a design parameter for Selective Laser Melting, In: Materials & Design 113 (1), (2017) S. 331–340.